Chapter 2
Material Models for Numerical Simulations

Abstract This chapter deals with the numerical simulations which are performed for terminal ballistics studies. These simulations are performed with specific codes which are designed to account for the high pressures which the impacting materials experience, and the high strain rates under which they are applied. The properties of the different materials are described by their equation of state and their constitutive relations, which characterize their high pressure properties and their yielding and failure modes, respectively. The experimental techniques, which are used to determine these properties, are also described here.

2.1 General Description

Numerical simulations of high velocity impact events are performed with large computer codes called hydrocodes, because their early use was for high pressure problems in which materials were treated as fluids. These codes can handle impulsive loadings which include shock waves with extremely high pressures and short rise times, as well as high temperatures and large deformations. Several review articles about hydrocodes and their use have been published over the past 30 years. As far as terminal ballistics is concerned, the reviews by Anderson (1987) and by Zukas (1990) are the most comprehensive and informative. The present chapter highlights some of the important issues concerning these codes for terminal ballistics studies. We follow Anderson's statement that "hydrocodes are the best instrumented experiment", since they can (and should) be used for sensitivity studies in terminal ballistics. These studies highlight the role of each parameter in the investigated process, and the physics behind the process is unveiled. Through the different issues presented in this book we shall demonstrate the construction and validation of analytical models with such sensitivity studies. As an example, consider the difficulty to determine experimentally the dependence of a projectile's penetration depth on the strength of the target. Any experimental attempt to vary only the strength of a target, within a large range of values, will result in some changes in its other properties as well. On the other hand, a series of simulations where only the strength of the target is varied systematically is easy to perform and it can offer the required

Z. Rosenberg and E. Dekel, *Terminal Ballistics*,
DOI 10.1007/978-981-10-0395-0_2

insight for this issue. Another important advantage of hydrocodes is that they can give information about events which are beyond any laboratory's performance. For example, the impact of meteors at velocities of 20–40 km/s cannot be studied in the laboratory but it can be easily investigated with these codes.

Basically, the hydrocode is an efficient and accurate scheme for solving the set of conservation equations for mass, momentum, and energy under the initial and boundary conditions which characterize the physical event. In addition to these equations and problem constraints, there are two sets of data which have to be specified for all the materials involved. These are the equation of state of the material and its constitutive relations, which were discussed briefly in Chap. 1. The equations to be solved describe the behavior of a continuum, but the code is solving them by discretization techniques for both space and time, through finite difference or finite element forms. With the finite difference technique, a grid is generated to represent material points for the given geometry of the participating bodies. The continuous spatial derivatives in the equations, like df/dx, are replaced by difference equations like $\Delta f/\Delta x$, where the differences Δx are related to the cell dimensions in the grid. The same ideas are applied to the differentiation with respect with time. Values of the parameters at a certain time (t) are calculated by their values at an earlier time $(t - \Delta t)$ and their corresponding time derivatives. With the finite element technique the actual differential equations are solved in small interconnected sub-regions (elements). Nodes are assigned to elements and an interpolation function is used to represent the variation of the variable over the element. Anderson (1987) discusses the four properties which have to be carefully considered in order to optimize these calculations, namely: consistency, accuracy, stability and efficiency.

The grids themselves are either Eulerian or Lagrangian and each type has its own merits and disadvantages. The Eulerian description has a spatial nature whereby the grid points and, consequently, the cell boundaries remain spatially fixed with time, while material can flow through the mesh. The net flow of material into this fixed cell volume determines its mass content, pressure, velocity etc. On the other hand, with the Lagrangian scheme, the grid is attached to the material and moves with it. With this scheme the grid points follow material paths, so it is more appropriate for cases where the material elements are less distorted. The Eulerian scheme is more useful for heavily distorted materials. An optimal combination for a situation where a rigid projectile is penetrating a soft target is obtained by using the Lagrange scheme for the projectile and the Euler scheme for the target.

One of the more important issues which have to be carefully considered is the issue of mesh size. Different results are obtained if the number of cells per unit length is not adequate. For example, it was found that for penetration studies with eroding long rods, the number of cells on the rod's radius should be at least eleven. The same density of cells should be kept in the target, at least for several projectile radii around its symmetry axis. In order to save computing time, the cell size at farther zones can be gradually increased according to their distance from the symmetry axis. The mesh cell size depends on the specific problem. As an example, a small cell size should be considered in cases where there is a fracture in the projectile or target. It is recommended that while preparing the code for its final runs, the numerical convergence

with respect to mesh cell size should be checked. Another important issue, especially when material elements are expected to deform considerably, is the issue of erosion with Lagrangian codes. At large deformations the code may run into trouble when treating heavily deformed elements. The use of the erosion threshold condition is then necessary in order to eliminate elements at a predetermined value of the plastic or geometric deformation. The erosion should be monitored constantly, and when it is too high one should replace the Lagrangian with an Eulerian code.

2.2 Material Properties

The high velocity impact of solid bodies can induce extremely high pressures and temperatures in both bodies, around their impact interface. These extreme conditions are propagated away from the impact area through strong shock waves, which eventually decay to elastic waves at large distances. During the short times, in which a solid experiences these high pressures and temperature it may undergo various physical changes, such as melting or evaporation, as well as mechanical changes which lead to strength loss, local fracture and even total shattering. Even though the state of the compressed solid under strong shock loading is an irreversible one, it is assumed to be of thermodynamic equilibrium nature. Thus, the thermodynamic states of the shocked solid, which are defined by its internal energy (e), specific volume (V) and the pressure (p), are assumed to lie on the equation of state surface, $e = e(V, s)$ or $e = e(V, T)$, where e and s are the internal energy and the entropy of the solid.

To summarize, the relevant material properties for terminal ballistics belong either to their equations of state (EOS), which account for material compression at high pressures and temperatures, or to their constitutive relations. These relations follow the strength and failure characteristics of the solid under high pressures, temperatures and strain rates, as well as during the large deformations which it experiences. This chapter describes some of the equations of state and the constitutive relations which are implemented in hydrocodes. These codes include a large data bank, which is continually updated, for the relevant parameters of the EOS and the constitutive properties for many materials.

2.2.1 The Equation of State

The equation of state (EOS) is a relation between the internal energy of the material, its density (or volume) and the pressure which characterize its state. The EOS is given through $e = e(\rho, p)$, or in terms of the corresponding compression curve $p = p(\rho, e)$. We have already seen that the Hugoniot relations result in compression curves which account for the state of the shocked material, $p_H = p_H(\rho, e_H)$, where the subscript H denotes a state on the Hugoniot. Other compression curves can be considered as special cases of the general EOS, such as the various isotherms $p = p$

(ρ), at a given temperature. The seminal work of P.W. Bridgman includes isotherms of many materials (both solids and liquids), compressed to 10 GPa, in the form:

$$\frac{\Delta V}{V_0} = -Ap + Bp^2 \tag{2.1}$$

where A and B are positive coefficients, characteristic to the material. The compressibility of the material is given by: β = A − BP, from which we find that B is the pressure derivative of the compressibility. Another relation for the isotherm is the Murnaghan equation which accounts for the data to much higher pressures. This relation is based on the assumption that the bulk modulus (K) increases linearly with pressure, thus: $K = K_0 + np$, where n is the pressure derivative of K. The resulting isotherms are expressed as:

$$p(\rho) = \frac{K_0}{n}\left[\left(\frac{\rho}{\rho_0}\right)^n - 1\right] \tag{2.2}$$

As was shown by Ruoff (1967), the value of n can be obtained by the relation n = 4S − 1, where S is the slope of the linear relation between the shock and particle velocities in (1.5). Using a typical value of S = 1.5, the value for n should be about 5.0, which is in accord with measured pressure derivatives of the bulk moduli for many solids.

In order to appreciate the relation between the Hugoniot and the room temperature isotherm, of a given material, consider the schematic description of these curves in Fig. 2.1. The points on the Hugoniot curve lie above the corresponding points on the isotherm, because of the higher temperatures which characterize the shocked state.

For a given value of the specific volume the following relation can be written for the points on the Hugoniot and the room temperature (T_0) isotherm:

$$p_H = p_{isoth} + p_T \tag{2.3}$$

where p_T is the thermal pressure. This is the extra pressure which is needed to compress the material to the volume V in order to overcome the temperature

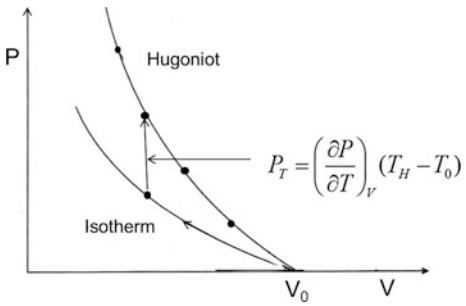

Fig. 2.1 A schematic description of the Hugoniot and isotherm curves

difference ($T_H - T_0$) between the Hugoniot and the isotherm. Written in another way, p_T can be expressed as:

$$p_T = \left(\frac{\partial p}{\partial T}\right)_V (T_H - T_0) \tag{2.4}$$

The partial temperature derivative of the pressure in (2.4), is a most important quantity in high-pressure physics, as is clearly evident from the above description. It was treated theoretically through solid-state physics considerations, in order to account for its experimentally observed values. As discussed by Zeldovich and Raizer (1965), this derivative is closely related to the volumetric derivative of the atomic vibration frequency around their equilibrium positions. With some simplifying assumptions, Gruneisen showed that:

$$\left(\frac{\partial p}{\partial T}\right)_V = \frac{\Gamma_{th} C_V}{V} \tag{2.5}$$

where C_v is the heat capacity of the material and Γ_{th} is the thermal Gruneisen coefficient, which is related to the above-mentioned atomic frequencies, and is defined by:

$$\Gamma_{th} = V\left(\frac{\partial p}{\partial e}\right)_V \tag{2.6}$$

These theoretical derivations led to one of the more useful equations of state, the Mie-Gruneisen equation, which is given by:

$$p = p_{ref} + \frac{\Gamma_{th}}{V}\left(e - e_{ref}\right) \tag{2.7}$$

where the current state of the material is related to some known (the reference) state through this simple relation. This equation of state is often used in the hydrocodes for deriving off-Hugoniot states, such as the release curves, while the Hugoniot relations are used in order to define the reference states. It turns out that Γ has a value of about 2.0 for many solids at ambient conditions. Moreover, Γ is assumed to be independent on temperature and it is also assumed that the product $\Gamma \cdot \rho$ is constant for a given solid, within a large range of pressures. Rosenberg and Partom (1982) demonstrated experimentally that this assumption holds for Plexiglas, by considering a somewhat different definition of Γ. This definition is given by:

$$\Gamma = -\left(\frac{\partial \ln T}{\partial \ln V}\right)_S \tag{2.8}$$

in which the partial derivative is defined along the isentropic compression curve of the solid. Rosenberg and Partom (1982) performed direct measurements of the

temperature rise and the volumetric strains, of isentropically compressed Plexiglas, by using in situ temperature and strain gauges. The isentropic loading of the specimen was achieved by a series of low amplitude shock reverberations in the specimen, and the gauges monitored its temperature and specific volume (strain) at each reverberation. Their main conclusion was that the product of $\Gamma \cdot \rho$ for Plexiglas is, indeed, constant within the range of their experiments.

2.2.2 The Constitutive Relations

The inclusion of the elastio-plastic behavior of solids into hydrocodes dates back to the early work of Wilkins (1964). His basic idea was to treat the elements of the stress tensor (σ_{ij}) as composed of two parts, the hydrostatic part (p) which is derived by the equation of state, and the deviatoric part (s_{ij}) which represents the geometric distortion of the material. Thus, according to this convention, the stress components are written as:

$$\sigma_{ij} = p \cdot \delta_{ij} + s_{ij} \tag{2.9a}$$

where δ_{ij} is the Kronecker delta. The rate of change in the deviatoric stresses is related to the strain rates through:

$$\dot{s}_{ij} = 2G\dot{\varepsilon}_{ij} \tag{2.9b}$$

where G is the shear modulus of the solid. These strain rates are decomposed to their elastic and plastic parts as follows:

$$\dot{\varepsilon}_{ij} = \dot{\varepsilon}^{e}_{ij} + \dot{\varepsilon}^{p}_{ij} \tag{2.9c}$$

Instead of working with tensors it is easier to use the equivalent (or effective) stress and strain measures, σ_{eq} and ε_{eq}, as defined by:

$$\sigma_{eq} = \sqrt{\frac{3 s_{ij} s_{ij}}{2}} \tag{2.10a}$$

$$\varepsilon_{eq} = \sqrt{\frac{2 \varepsilon_{ij} \varepsilon_{ij}}{3}} \tag{2.10b}$$

with which the constitutive relations are written in the form: $\sigma_{eq} = \sigma\left(\varepsilon_{eq}, \dot{\varepsilon}, T\right)$.

Wilkins (1964) showed that it is easier to work within the stress space where the axes are along the principal stresses of the problem, denoted by σ_1, σ_2, and σ_3. The diagonal line in this three dimensional stress space, for which $\sigma_1 = \sigma_2 = \sigma_3$, denotes states on the hydrostatic pressure loading of the material. The equivalent stress is a measure for the distance of a given point in this space from the diagonal line.

The various yield criteria define the maximum permissible value of this distance. Thus, in terms of the principal stresses the border between elastic and plastic states is a cylindrically shaped envelope, around the diagonal line which corresponds to the hydrostatic loading conditions. All the states inside this yield envelope correspond to the solid's elastic range, while those on the envelope correspond to its plastic (yielded) states. By definition, the states which correspond to points outside this yield envelope are not permissible. Wilkins (1964) suggested the radial return procedure, by which these states should be brought to the yield envelope in numerical simulations.

The equation for the yield surface in the principal stress space is given by:

$$(\sigma_1 - \sigma_2)^2 + (\sigma_2 - \sigma_3)^2 + (\sigma_3 - \sigma_1)^2 = 2Y^2 \tag{2.11a}$$

or, in its deviatoric form:

$$s_1^2 + s_2^2 + s_3^2 = \frac{2}{3}Y^2 \tag{2.11b}$$

The various yield criteria are, in fact, imposing a maximum value for this equivalent stress which has to be specified in the code. For example, the well-known von-Mises criterion states that the equivalent stress of the material cannot be higher than its yield strength under simple tension, $\sigma_{eq} \leq Y_0$. In terms of the yield surface in the stress space, this criterion is represented by the surface of a cylinder with a radius of Y_0, which surrounds the main diagonal ($\sigma_1 = \sigma_2 = \sigma_3$). The von-Mises criterion accounts for the yielding behavior of many metals and alloys which exhibit elastic-perfectly-plastic characteristics. This is true for high strength materials, such as armor steels and the strong aluminum alloys. Softer metals often show an appreciable strain hardening behavior where the strength is a strong function of the strain. The stainless steel 304L is an example for a significantly hardening material, since its strength increases by a factor of five under plastic strains of 50 %. On the other hand, steels which are referred to as rolled homogenous armor, show an almost ideal elastic-plastic behavior with no strain-hardening. One should note that the interaction between a penetrating projectile and a target is always accompanied by large strains in both materials. Thus, it is the stress at large strains, the so-called "flow stress", which is the important strength property of the material for terminal ballistics. The relevant strain rates for impacts at ordnance velocities (up to about 2.0 km/s) are 10^3–10^4 s^{-1}. These are the rates covered by the Kolsky bar system which is the main reason for its extensive use. One has to consider the fact that the strength of most solids increases at high confining pressures, while high temperatures reduce their strength (thermal-softening). Thus, a complete constitutive relation for the strength of the solid should include all the data concerning the effects discussed here. Some of these constitutive models, which are implemented in hydrocodes, are described next.

The constitutive equation proposed by Johnson and Cook (1983) is one of the more popular in the field of terminal ballistics. This equation, which is referred to as the JC model, includes the effects of plastic strain, strain rate, pressure, and temperature on the material strength, as follows:

$$Y = \left[A_1 + A_2 \varepsilon_p^n\right] \cdot \left[1 + A_3 \ln\left(\dot{\varepsilon}_p^*\right)\right] \cdot \left[1 - T_H^m\right] \tag{2.12}$$

where A_1, A_2, A_3, n and m, are material constants. ε_p is the equivalent plastic strain, and $\dot{\varepsilon}_p^* = \dot{\varepsilon}_p / \dot{\varepsilon}_0$, is the normalized plastic strain rate with $\dot{\varepsilon}_0 = 1.0\,\mathrm{s}^{-1}$ as the reference rate. The homologous temperature (T_H) is defined by the room and melting temperatures (T_{room} and T_m), according to:

$$T_H = \frac{T - T_{room}}{T_{melt} - T_{room}} \tag{2.13}$$

Another material model which is frequently used for high pressure impacts is the rate-independent model of Steinberg (1987). According to this model the changes in the flow stress (Y), with high pressures and temperatures, are equal to the corresponding changes in the shear modulus (G) of the material. The relations for Y(p, T) and G(p, T) are given by the following expressions:

$$Y(p,T) = Y_0 \cdot \frac{G(p,T)}{G_0}\left(1 + \beta_p \varepsilon\right)^n \tag{2.14a}$$

$$G(p,T) = G_0 \cdot \left[1 + \frac{G'_p}{G_0} \cdot \frac{p}{\eta^{1/3}} + \frac{G'_T}{G_0}(T - 300)\right] \tag{2.14b}$$

where β_p and n are material parameters, ε is the effective plastic strain and $\eta = \rho/\rho_0$ is the compression ratio of the solid. The primed parameters, with the subscripts p and T, are the derivatives of G with respect to pressure and temperature, respectively, at the reference state (T = 300 K, p = 0).

A third family of constitutive equations is due to Zerilli and Armstrong (1987), shortly termed the ZA model. Unlike the JC model, which is basically an empirical one, the constitutive equations of the ZA model are based on dislocation dynamics theory. They treat face centered (FCC) and cubic centered (BCC) metals differently, since the rate and temperature sensitivities are very different for these two families of materials. Their constitutive equations are given by:

$$\sigma_{eq} = \sigma_0 + k d^{-0.5} + C_2 \varepsilon^{0.5} \exp[-C_3 T + C_4 T \ln \dot{\varepsilon}] \quad \text{For FCC materials} \tag{2.15a}$$

$$\sigma_{eq} = \sigma_0 + k d^{-0.5} + C_1 \exp[-C_3 T + C_4 T \ln \dot{\varepsilon}] + C_5 \varepsilon^n \quad \text{For BCC materials} \tag{2.15b}$$

where $C_1 \ldots C_5$ and n are material parameters. The Hall-Petch relation, between the strength of a metal and its average grain diameter (d), has been taken into account in this formulation.

2.2.3 *Failure of Ductile Materials*

The models described above treat the changes in the material's effective strength through its hardening and softening mechanisms. The characterization of these changes is important for ductile materials which can withstand large plastic strains before they fail. Ductile materials fail either under tension or by shear when a certain threshold strain is reached. The failure of a specimen is defined by the loss of cohesion in its interior, leading to either its complete disintegration or to some inner damage, which is manifested by the appearance of new free surfaces inside the specimen. Fracture under tension is the end result of the coalescence of small voids, forming macroscopic free surfaces inside the specimen. The processes of void nucleation and growth in ductile materials, under dynamic loading conditions, have been investigated by many workers and the review article of Curran (1982) gives a comprehensive account of this field. Fracture under shear is usually the end result of the appearance of shear bands in the specimen at the highest shear locations. These bands are very narrow zones in which voids are eventually developed, leading to failure by their coalescence when the shear strains in the bands exceed their limiting values. In contrast, brittle materials fail within their elastic response regime, with negligible straining, and their main mode of failure involves microcrack nucleation and coalescence, as discussed in the next section.

Johnson and Cook (1985) proposed a fracture criterion for ductile materials, which is especially suited for numerical codes. This criterion is based on the maximum strain to fracture (ε_f) of an element, which depends on its strain path, strain-rate, and temperature. It also depends on the stress triaxiality, which is defined by $\sigma^* = \sigma_m/\sigma_{eq}$, where σ_m is the local pressure as calculated by the average of the three principal stresses in each element. This is a very important parameter, since the propensity of ductile materials to fail is strongly dependent on the pressure exerted on them. Compressive stresses tend to prevent failure by closing voids and microcracks, while tensile stresses enhance failure by further opening them. The influence of stress triaxiality according to various models is based on the void growth model of Rice and Tracey (1969). Different stress triaxialities are not easily achieved in well defined experiments, since it is difficult to accurately define the real state of a specimen, especially under complex loading situations. One of the more popular techniques for generating different stress triaxialities, which was suggested by Bridgman (1952), is based on varying the notch radius in the mid-section of a tensile specimen. This is a relatively simple and straightforward technique which is easy to analyze through numerical simulations.

The dependence of fracture strain on the stress triaxiality for the structural steel Weldox 460E, as obtained by Hopperstad et al. (2003), is shown Fig. 2.2. Note that

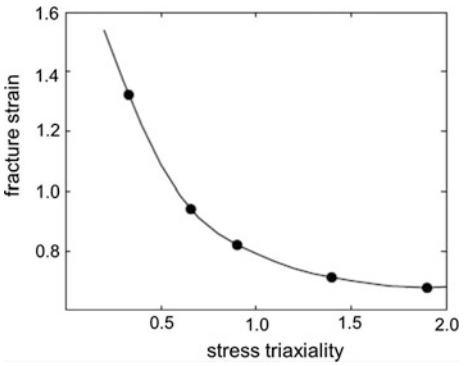

Fig. 2.2 The dependence of fracture strain on the stress triaxiality for Weldox 460E steel

according to this representation, tensile and compressive stresses correspond to positive and negative triaxialities, respectively, while pure shear corresponds to zero triaxiality. Obviously, under compressive stresses the fracture strain increases markedly with stress triaxiality since high pressures oppose the opening of voids and cracks. In fact, there are some models according to which these graphs rise asymptotically to infinite fracture strains at a compressive triaxiality of $\sigma^* = -1/3$.

The JC failure model defines a continuous degree of damage (D_f), in the element under consideration, which is given by:

$$D_f = \sum \frac{\Delta \varepsilon_{eq}}{\varepsilon_f} \tag{2.16}$$

where $\Delta\varepsilon_{eq}$ is the increment of accumulated equivalent plastic strain during an integration cycle and ε_f is the equivalent plastic strain at fracture. This value is reached when the damage function (D_f) reaches the value of 1.0. The failure strain is given by the following functional form:

$$\varepsilon_f = [D_1 + D_2 \exp(D_3 \sigma^*)] \cdot \left[1 + D_4 \ln\left(\dot{\varepsilon}_p^*\right)\right] \cdot [1 + D_5 T_H] \tag{2.17}$$

where $D_1 \ldots D_5$ are constants which have to be calibrated for each material. Many of the constants which appear in these constitutive equations, for strength and failure, are determined by the Kolsky bar system described in Chap. 1.

Typical examples of dynamic stress-strain curves for three aluminum alloys are given in Fig. 2.3, as obtained by the Kolsky bar system in our laboratory. Note that the 6061-T6 alloy exhibits a truly ductile behavior, where the specimen does not fail even at compressive strains as high as 0.8. On the other hand, the stronger alloys 2024-T3 and 7075-T6, show a clear softening behavior at strains of about 0.6 and 0.4, respectively. These strong alloys fail at much higher strains under static loading, which is an indication for a thermal softening effect operating at high strain rates, as discussed by Rosenberg and Ashuach (2014). They showed that these strength decreases can be related to the fact that the specimens reach a temperature

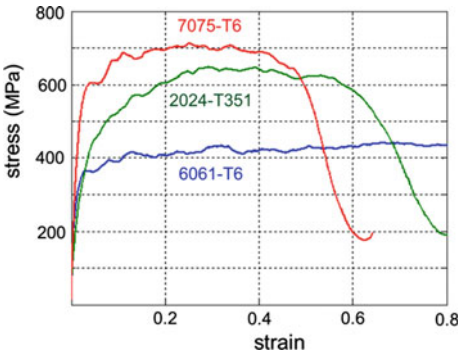

Fig. 2.3 Dynamic stress–strain curves for three aluminum alloys loaded in the Kolski bar

of about half their melting temperatures. At these high temperatures they lose a significant amount of their strength, which leads to subsequent deformation followed by even higher temperatures. Note that the flow stresses of these alloys, at strain rates of about 10^3 s^{-1}, are: Y = 0.42, 0.62 and 0.7 GPa, for the 6061-T651, 2024-T351 and 7075-T6 alloys, respectively. These are the appropriate values which one should use for their compressive strength in numerical simulations which follow terminal ballistics events, especially if the simple von-Mises criterion is used.

A dynamic stress–strain curve for a specimen of the titanium alloy Ti-6Al-4V, which was compressed by the Kolsky bar in our lab, is shown in Fig. 2.4. One can see that at a compressive strain of about 20 % the disc shaped specimen lost its load capacity. The failure resulted in two pieces of the disc which were separated by a fracture along its diagonal. The early failure of this alloy is attributed to its propensity to fail by adiabatic shearing, which has been investigated by numerous researchers over the years, as reviewed by Bai and Dodd (1992). Next we summarize, briefly, some of the main results from these studies.

The dynamic failure of metals and alloys under impulsive loading conditions is usually manifested by gross shearing at material interfaces, as a result of large velocity gradients at those locations. In many cases these large shear strains appear

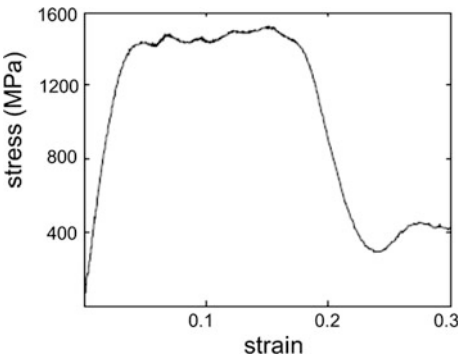

Fig. 2.4 The dynamic stress–strain curve for the Ti-6Al-4V alloy

in very narrow bands which have been termed adiabatic shear bands (ASB). This failure mechanism, which is believed to be due to thermo-mechanical instabilities, is one of the more common failure modes under dynamic loading at strain rates of about 10^3 s^{-1}. The narrow shear bands often contain material which experienced a structural phase transformation, in which case they are referred to as transformation bands. The phenomenon of adiabatic shear banding received a lot of attention because of their importance for both military and industry applications. Bai and Dodd (1992) summarize much of the data and the analysis concerning this phenomenon. Important articles concerning the nature of ASBs are those of Staker (1981), Rogers (1983), Timothy and Hutchings (1985), and Giovanola (1988a, b). Although many aspects of this issue have been highlighted in these studies, its physical picture is not complete because, in addition to the instabilities involved, the shear bands often include microcracks or microvoids which initiate and grow during band evolution. The work of Giovanola (1988a, b), on 4340 steel under pure shear, highlights the interconnection between the thermo-mechanical shear instability, which acts at the first stage of the process, and the subsequent coalescence of microvoids which leads to fracture within the band at the second stage. These stages are clearly seen in the work of Xue et al. (2002) who performed radial collapse experiments with titanium and Ti-6Al-4V alloy specimens, and followed the evolution of shear bands. In these experiments hollow cylinders are subjected to a pressure impulse by a surrounding explosive layer. The recovered cylinders are examined for the number, length and spacing of the shear bands. Figure 2.5 shows

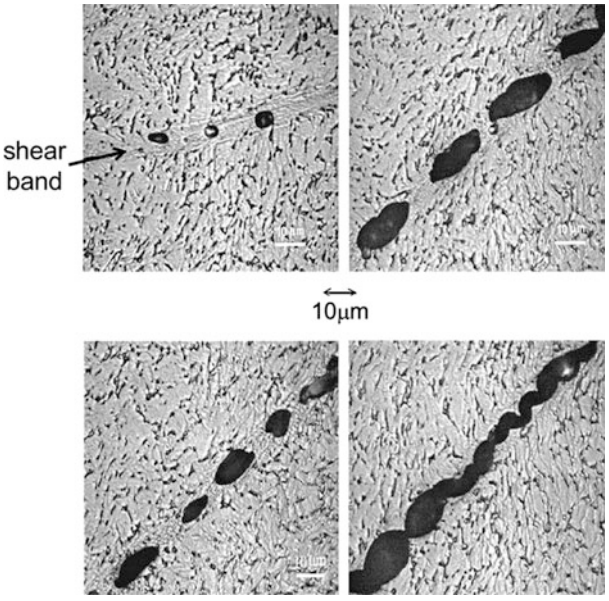

Fig. 2.5 Void nucleation and growth within shear bands in thick-wall collapsing Ti-6Al-4V specimens

shear bands in specimens of the titanium alloy which were subjected to different strains. One can clearly follow the sequence of events in which, at low strains the voids nucleate within the band as a result of tensile stresses, and for larger compressions (strains) they grow and eventually coalesce. The interesting observation from these pictures is that the voids form within the band boundaries, due to tensile stresses which develop during the strong shearing of these bands. Other materials, especially strong steels, exhibit a similar evolution of the process with microcracks, rather than microvoids, initiating in the shear bands.

In all of these works the initiation of shear bands has been treated through the classical work of Zener and Hollomon (1944), who proposed a mechanism for the thermo-mechanical instability which initiates them. The analysis starts by writing the differential for the shear stress, $\tau = \tau(\mathrm{T}, \varepsilon, \dot{\varepsilon})$, which depends on the temperature, strain, and strain rate in the solid, in the following way:

$$d\tau = \left(\frac{\partial \tau}{\partial T}\right)_{\varepsilon,\dot{\varepsilon}} dT + \left(\frac{\partial \tau}{\partial \varepsilon}\right)_{\dot{\varepsilon},T} d\varepsilon + \left(\frac{\partial \tau}{\partial \dot{\varepsilon}}\right)_{\varepsilon,T} d\dot{\varepsilon} \tag{2.18a}$$

from which one obtains:

$$\frac{d\tau}{d\varepsilon} = \left(\frac{\partial \tau}{\partial T}\right)_{\varepsilon,\dot{\varepsilon}} \frac{dT}{d\varepsilon} + \left(\frac{\partial \tau}{\partial \varepsilon}\right)_{\dot{\varepsilon},T} + \left(\frac{\partial \tau}{\partial \dot{\varepsilon}}\right)_{\varepsilon,T} \frac{d\dot{\varepsilon}}{d\varepsilon} \tag{2.18b}$$

The instability condition is defined by $d\tau/d\varepsilon = 0$ which, for a constant strain rate experiment, occurs when:

$$\left(\frac{\partial \tau}{\partial \varepsilon}\right)_T = -\left(\frac{\partial \tau}{\partial T}\right)_\varepsilon \left(\frac{d\varepsilon}{dT}\right)^{-1} \tag{2.19}$$

Since these bands form under adiabatic conditions the generated heat cannot diffuse out of the bands themselves. Thus, one can write the following equation for the temperature rise in the bands, due to their plastic deformation:

$$\rho C_v dT = \tau d\varepsilon \tag{2.20a}$$

where ρ is the density of the specimen and C_v is its specific heat. From this relation one obtains:

$$d\varepsilon/dT = \rho C_v/\tau \tag{2.20b}$$

In order to predict the critical shear strain for adiabatic shearing from these equations, one needs to have the constitutive equation for the material. Assuming a power law dependence of the shear stress on shear strain, such as $\tau = \mathrm{N} \cdot \varepsilon^{\mathrm{n}}$, the

threshold value of the strain (ε_i) which marks the onset of thermo-mechanical instability, is given by:

$$\varepsilon_i = n\rho C_v \left(\frac{\partial \tau}{\partial T}\right)_{\varepsilon,\dot{\varepsilon}} \tag{2.21}$$

which has been shown to account for the experimental results in many cases, but not for all of them, as discussed by Bai and Dodd (1992) and by Woodward (1990) who summarizes other approaches to the issue of adiabatic shear. Some confusion about the true nature of adiabatic shear bands arises from the fact that in many cases they appear in specimens with sharp corners, where a geometrically forced stress-concentration is responsible for the shear failure. This issue will be further discussed in Chap. 4, where we highlight the importance of adiabatic shearing for plate perforation by flat-nosed projectiles.

A somewhat different loading history of specimens in the Kolsky bar system is obtained by the so called upsetting (or multi-step) test. In these tests the disc shaped specimen is loaded to a relatively small strain, so that it does not experience a significant temperature rise. After some time it is then reloaded, again to a small strain, and the procedure is repeated several times. In fact, this is a dynamic loading with practically no heating, and the specimen is supposed to withstand much larger strains without failure. Ashuach and Rosenberg (2014) performed such multi-step loadings on several metals and alloys and observed the differences between their stress-strain curves under single and multi-step loadings. Figure 2.6 shows the stress-strain curves for specimens of Al 2024-T351, subjected to single and multi-step loadings. It is clearly seen that the specimen loaded by a single step, at a strain rate of 5×10^{-3} s^{-1}, experienced thermal softening at a strain of about 0.6. On the other hand, the multi-step loading did not result in a loss of strength even at a strain of 0.8. In fact, the stress-strain curve under multi-step loading is very similar to the quasi-static curve, as expected, since the temperature rise has to be very small under multi-step loading.

Rosenberg and Ashuach (2014) showed that for several metals and alloys, the compressive strains where thermal softening occurs, can be estimated by

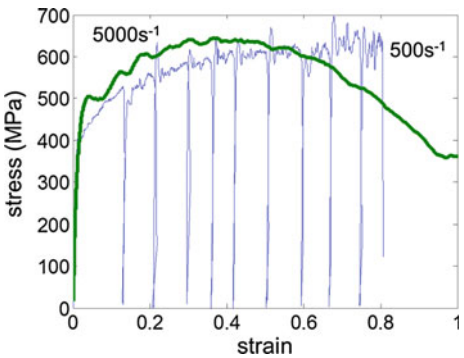

Fig. 2.6 The response of Al2024-T351 specimens to single and multi-step loadings

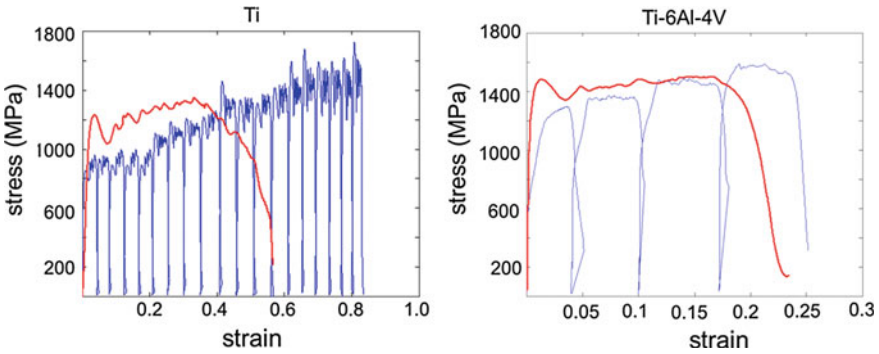

Fig. 2.7 The response of pure titanium (*left*) and the alloy (*right*) to single and multi-step loadings

considering the temperature rise due to the deformation work. When the temperature of the specimen reaches a certain threshold temperature the specimen's strength is expected to decrease, and thermal softening sets in. These threshold temperatures, for various metals and alloys, can be determined by static compression tests under various temperatures. As a rough estimate the softening threshold temperatures are equal to about half the respective melting temperature of the specimen. These materials showed no failure even at high strains when loaded by the multi-step technique. On the other hand, multi-step loading of the titanium (Ti-6Al-4V) and magnesium (AM50) alloys resulted in nearly the same failure strains as in the single-step loading. Figure 2.7 shows the results of these tests for pure titanium and its alloy from single and multi-step loadings, from Ashuach and Rosenberg (2014). The difference between these responses is very clear. The pure titanium shows the typical response for most materials tested by Ashuach and Rosenberg (2014), with a clear indication for thermal softening in the single step loading. The multi-step loading of the pure titanium specimen shows no indication for failure even at much higher strains. On the other hand, the multi-step loaded Ti-6Al-4V specimen failed during the fourth loading step, at a compressive strain which is very close to the failure strain under single loading, as seen in the figure. Since each loading step is assumed to induce a very low temperature rise in the specimen, we may consider this procedure as quasi isothermal. These results for the titanium and magnesium alloys, in Ashuach and Rosenberg (2014), show that the failure of these alloys is not related to the temperature rise which accompanies the dynamic loading. Hence, one should look for other causes for the propensity of these alloys to fail at low strains by adiabatic shearing.

The adiabatic shear failure is a very important issue in terminal ballistics because it can affect the capability of the target to withstand the attack of a projectile. As we shall see in Chap. 4, this is a real concern for high-strength-targets whose thickness is of the order of the projectile's diameter. Figure 2.8, from Olson et al. (1980), demonstrates this issue very well. Here we see the end results of impacts by high strength steel projectiles at two plates of 4340 steel, which have very different

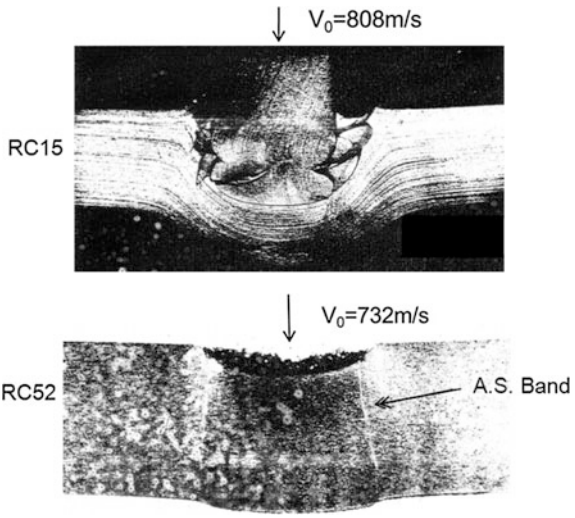

Fig. 2.8 Different failure mechanisms in steel plates of different strength

hardness (strength). The low-strength steel plate (Rockwell hardness RC-15) deformed heavily and was able to absorb the projectile's kinetic energy through this large deformation. On the other hand, the high-strength plate (Rockwell hardness RC-52) was hardly penetrated but it developed a shear band extending almost to its back surface. Clearly, at a somewhat higher impact velocity this plate would be penetrated, with a shear plug ejected from it. Thus, the high-strength plate is less efficient in this case, due to its propensity to fail by adiabatic shear. The white color of shear bands in steels is usually observed by the etching process of sectioned plates.

2.2.4 Failure of Brittle Materials

The dynamic behavior of brittle materials, such as glass and ceramics, is quite different and more complicated than that of ductile metals and alloys. First, there is a large difference between the compressive and tensile strengths of a brittle solid, which can reach a factor of 10 and more. By definition, brittle solids fail within their elastic range of response, with practically no plastic straining. Their failure behavior is pressure dependent, with relatively very small (if any) strain rate sensitivity. Also, the damaged zone in a brittle material can spread from the impact point, through cracks which run in all directions, affecting the properties of a large volume in the brittle solid. The various constitutive equations which describe the failure thresholds of brittle materials, are based on the classical work of Griffith (1920, 1924), who analyzed the stresses around an open elliptic flaw in a plate under biaxial stress loading. Griffith followed the analysis of Inglis (1913), who showed that even when the far end stresses are compressive, the stresses at the tips of the flaw are tensile.

With increasing stress at the plate boundaries, these tensile stresses around the crack, reach a critical value (σ_0) which is a material property, leading to uncontrolled crack growth. The value of σ_0 according to this analysis is equal to the tensile strength of the material under uniaxial loading. Denoting the two far-end stresses which act on the plate as σ_1 and σ_2, Griffith derived the following relations expressing the critical conditions for the brittle failure:

$$\sigma_2 = \sigma_0 \quad \text{if: } 3\sigma_2 + \sigma_1 > 0 \tag{2.22a}$$

$$(\sigma_1 - \sigma_2)^2 = -8\sigma_0(\sigma_1 + \sigma_2) \quad \text{if: } 3\sigma_1 + \sigma_2 < 0 \tag{2.22b}$$

where tensile stresses are positive, and compressive stresses are negative in this formulation. These equations give the failure envelope of a brittle solid in the (σ_1, σ_2) plane, as shown in Fig. 2.9. All the states which are described by points inside the two curves correspond to intact material, while those outside the curves correspond to failure situations. Hydrostatic compressions, which correspond to the third quadrant in this figure, enhance the integrity of the brittle solid, as expected. According to Griffith's model the critical tensile strength (σ_0) of the solid is smaller by a factor of 8 than its compressive strength under uniaxial stress loading. Later works, by McClintock and Walsh (1962) for example, resulted in a factor of 10 between these two strength thresholds. Other refinements of these models, as well as data for concrete and rocks, can be found in Paterson (1978).

The Griffith failure criterion which, in effect, defines the strength of a brittle solid under compression and tension, is very different from the various yield criteria for ductile materials which were discussed above. Thus, the relation between the Hugoniot elastic limit (HEL) of a brittle solid and its dynamic strength (Y_d) should

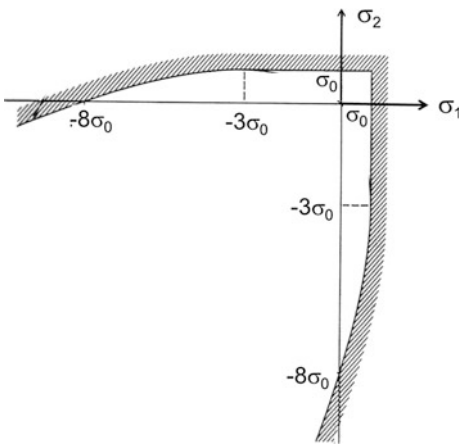

Fig. 2.9 The failure envelope for brittle materials, according to Griffith's theory

be different than the corresponding relation, (1.7), for ductile materials, which follows the von-Mises yield criterion. The relation for brittle solids should be based on the Griffith criterion, (2.22), with which Rosenberg (1993) derived the following relation:

$$Y_d = \frac{(1-2\nu)^2}{1-\nu} \cdot HEL \tag{2.23}$$

where ν is Poisson's ratio of the brittle material. With the Griffith criterion, the dynamic strength of a brittle specimen is smaller by a factor of $(1 - 2\nu)$ than the strength deduced from (1.6), which is based on the von-Mises yield criterion.

The first numerical simulations for terminal ballistics applications involving ceramic tiles were performed in the late 1960s by M.L. Wilkins and his colleagues, as described by Wilkins (1978). This work will be described in the third part of this book, where we review the issue of ceramic armor. The failure criterion in Wilkins' work was based on a maximum tensile strength, which was set at $\sigma_0 = 0.3$ GPa in his simulations. The first implementation of the Griffith model itself, for ceramic tiles in terminal ballistics simulations, was by Mescall and Tracy (1986). Johnson and Holmquist (1990, 1993) further developed the Griffith model and included a damage function at every time step in the simulation. The various parameters in the first version of their model (JH-1) are shown in Fig. 2.10, for the equivalent strength of a brittle material. The model assumes that the tensile strength (spall) is much lower than the compressive strength, and that the fractured material has lost its tensile strength completely. The compressive strength of both intact and damaged materials are linearly dependent on pressure at the low pressure range, and reach asymptotic values which depend on the strain rate. The damage function is calculated continuously at each time step in the simulation, and it lowers the strength of the failed material. This model will be further discussed in Chap. 6 where we deal with ceramics for armor applications.

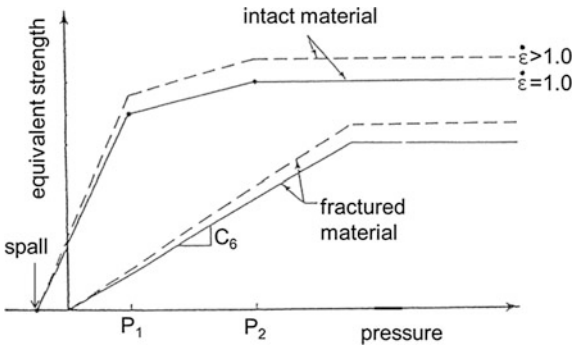

Fig. 2.10 The JH-1 model for the equivalent strength of brittle materials

2.2.5 The Spall Failure

It was noted earlier that spalling is a unique failure phenomenon, which takes place under dynamic conditions. When shock waves are reflecting from free surfaces as release waves, they induce tensile stresses in the solid. If the amplitude of these tensile waves is high enough the material fails and a spall is created near its free surface. The relevance of this mode of failure for terminal ballistics can be seen in sectioned targets, which have been impacted by relatively blunt projectiles at high impact velocities. For example, the spall in an annealed 1100 aluminum plate impacted by a glass sphere, from the work of Horz et al. (1994), is clearly seen Fig. 2.11. The diameter of the sphere (3.18 mm) was about a quarter of the plate thickness, and its impact velocity was 6.0 km/s.

The study of spall failure in solids has been the focus of a large amount of research for over 50 years. The early models assigned a threshold tensile strength to the specimen, which was calibrated by one-dimensional shock wave experiments, as discussed in Chap. 1. Subsequent developments showed that the spall process is more complicated, and that its time dependence should be taken into account, as was noted by Tuler and Butcher (1968). Many models were developed in order to account for this type of failure and the article of Curran (1982) describes those which are based on the nucleation of defects and their growth (the so called NAG models). The time dependence of the spall process leads to scaling effects which were the focus of an intense research by Russian researchers, as summarized by Ogorodnikov et al. (1999). A particularly thorough work on this issue is that of Al'tshuler (1966), where the reciprocal relation between the critical tensile stress and its duration is very clearly demonstrated. The dependence of the spall failure on the tensile impulse, rather than on a threshold stress, has been highlighted by Gray et al. (2007). They showed that a square-shaped tensile pulse and a triangular-shaped pulse can cause the same amount of incipient spall, if they induce a similar tensile impulse at the spall plane in the specimen. Thus, according to Gray et al. (2007), the tensile impulse is the important factor for the spall phenomenon, rather than the amplitude of the tensile wave.

Grady (1988) proposed energy balance considerations to establish the loading conditions at which spall occurs. This approach accounts for the transition between

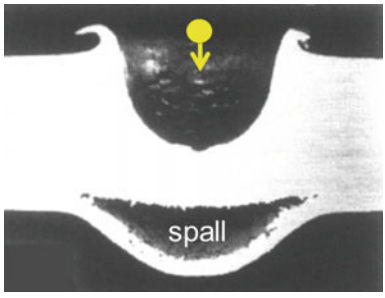

Fig. 2.11 Spall failure in an aluminum plate impacted by a glass sphere at 6.0 km/s

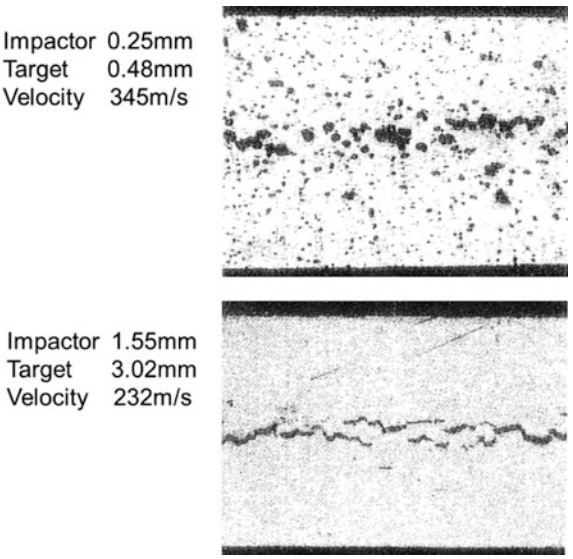

Fig. 2.12 Different void shapes in aluminum alloy plates subjected to tensile pulses of different durations

brittle and ductile spall failures, which has been observed for several materials when the loading conditions are changed. As an example, consider the sectioned 6061-T6 aluminum targets from the plate-impact experiments of Christman et al. (1971), as shown in Fig. 2.12. A marked difference in the void shape is clearly seen in these plates, which were subject to tensile stresses of different durations and rates. The round shaped voids, in the specimen at the top, suggest a ductile spall mechanism for the shorter pulse duration (higher rate). On the other hand, a brittle spall is evident in the cross section of the specimen at the bottom of the figure, which was subjected to a tensile pulse of a longer duration (and lower rate). The different loading rates in the two experiments resulted in from the different thicknesses of the impactor and the target in these experiments. Note that in both cases the specimens are only partially spalled, a phenomenon which is termed "incipient spall". A full spall process is characterized by the complete coalescent of the voids, leading to a clear opening inside the specimen, as shown in Fig. 2.11.

The analysis of Grady (1988) is based on macroscopic material properties, such as the fracture toughness and the flow stress of the material, resulting in a predictive tool for the occurrence of spall under given loading conditions. This analysis leads to the following relations between the spall strengths for both ductile and brittle materials, and their relevant properties and loading conditions:

$$P_{spall} = \left(3\rho C_0 K_c^2 \dot{\varepsilon}\right)^{1/3} \quad \text{For brittle spall} \tag{2.24a}$$

$$P_{spall} = \left(2\rho C_0 Y \varepsilon_f\right)^{1/2} \quad \text{For ductile spall} \tag{2.24b}$$

where ρ and C_0 are the specimen's density and sound speed, respectively, Y is its flow stress and K_c is its fracture toughness. The strain rate ($\dot{\varepsilon}$) in the experiment is important for the brittle fracture, while the strain to failure (ε_f) plays an important role for the ductile failure mode.

Rosenberg (1993) analyzed the spall failure in brittle materials through the Griffith failure criterion and derived the following relation between the spall strength and the Hugoniot elastic limit (HEL) of the solid:

$$\sigma_{spall} = \frac{(1-2\nu)^2}{8(1-\nu)} \cdot HEL \tag{2.25}$$

where ν is the Poisson ratio of the solid. This expression results in factors of 15–25 between the HEL and the spall strength of brittle materials, having Poisson's ratios in the range of ν = 0.15–0.25. Such factors are often measured for strong ceramics, having spall strengths of 0.3–0.6 GPa and HEL values in the range of 6.0–15.0 GPa.

A rather simple model for the spall strength of ductile materials was proposed by Rosenberg (1987). This model is based on the cavity expansion analysis of Bishop et al. (1945), for the minimal pressure which has to be applied on the walls of a small cavity, in an elasto-plastic solid, in order to expand its volume indefinitely. The cavity expansion analysis will be described in detail in Chap. 3. It deals with a large elasto-plastic solid with a small cavity inside. Pressure is introduced in the cavity and the analysis deals with the state of the solid, around the cavity, as the pressure is increased. As will be shown later, there is a threshold pressure which drives the cavity indefinitely. This is similar to the elongation of a tensile specimen of an elasto-plastic material, when the stress reaches its yield value. The threshold pressure depends on the elastic properties of the solid (Young's modulus E, and Poisson's ratio ν), as well as on the solid's strength. Assuming that spall is initiated by a process which is similar to the cavity expansion process, Rosenberg (1987) derived the following expression for the spall strength of ductile solids:

$$\sigma_{spall} = \frac{2Y}{3}\left[2 + \ln\left(\frac{E}{3(1-\nu)Y}\right)\right] \tag{2.26}$$

where E, ν and Y are the Young's modulus, Poisson's ratio and the strength of the solid, respectively. The predicted spall strengths of various materials, as calculated by this expression, were found to be close to their experimental results. For example, this expression results in: σ_{spall} = 1.7, 3.6 and 4.6 GPa, for an aluminum alloy with strength of Y = 0.4 GPa, steel with Y = 0.8 GPa and the titanium alloy Ti/6Al/4V with strength of Y = 1.2 GPa, respectively. These values are very close to the experimentally derived spall strengths of these materials. As mentioned above, the cavity expansion process and its relevance to penetration mechanics will be discussed in Chap. 3.

http://www.springer.com/978-981-10-0393-6

Terminal Ballistics

Rosenberg, Z.; Dekel, E.

2016, XIV, 359 p. 272 illus., 13 illus. in color., Hardcover
ISBN: 978-981-10-0393-6